Astroparticle Physics

Lectures:

05.02.2019 1. Historical introduction, basic properties of cosmic rays
07.02.2019 2. Hadronic interactions and accelerator data
19.02.2019 3. Cascade equations
21.02.2019 4. Electromagnetic cascades
26.02.2019 5. Extensive air showers
28.02.2019 6. Detectors for extensive air showers
09.04.2019 7. High energy cosmic rays and the knee in the energy spectrum of cosmic rays
16.04.2019 8. Radio detection of extensive air showers
25.04.2019 9. Acceleration, astrophysical accelerators and beam dumps
07.05.2019 10. Extragalactic propagation of cosmic rays
16.05.2019 11. Ultra high energy cosmic rays
21.05.2019 12. Astrophysical gamma rays and neutrinos
28.05.2019 13. Neutrino astronomy
04.06.2019 14. Gamma-ray astronomy

http://particle.astro.ru.nl/goto.html?astropart1819

lecture 12
Astrophysical gamma rays and neutrinos
Gaisser chapter 11

In this chapter we focus on gamma rays as probes of cosmic ray propagation in the Galaxy. Because photons are neutral, they point back to their origin, either in individual sources or from interactions of cosmic rays in the interstellar medium. Protons produce gamma rays primarily via $\pi^0 \rightarrow \gamma\gamma$. Electrons produce gamma rays primarily by bremsstrahlung and by inverse-Compton scattering (up-scattering of optical or other lower-energy photons). In this chapter we illustrate the basic ideas in the context of the simple model of the Galaxy described in Chapter 9.

Discussion: The GALPROP code, developed over the past two decades, provides a comprehensive framework for studies of cosmic ray transport and diffuse gamma-ray production. Its general framework is the diffusion model described in Chapter 9; however, it is much more general and handles more details than the simple discussion presented in this chapter. For example, the complex structure of the Galaxy is accounted for, and parameters of the diffusion equations can be modified as well as assumptions about the properties of the interstellar medium and the structure of the galactic halo, galactic winds, convection, reacceleration, etc. The code is publicly available (http://galprop.stanford.edu), and its physics is reviewed in [341].

11.1 γ-rays from decay of π^0

We begin with what is the biggest source of diffuse gamma radiation in the disk of the Milky Way; namely, neutral pions from cosmic ray interactions with gas in the interstellar medium. The neutral pion emissivity (defined as particles produced per second per hydrogen atom) is (by analogy with Eq. 5.70)

$$q_{\pi^0} = 4\pi\, \sigma_{pp} \left\{ Z_{p\pi^0} \right\} N_0(E_\pi), \tag{11.1}$$

where $N_0(E_\pi)$ from Eq. 5.8 is the power-law approximation for the differential spectrum of nucleons evaluated at the energy of the pion and the factor 4π accounts for the isotropic flux of nucleons in the disk of the Galaxy. The convolution with kinematics for the decay $\pi^0 \rightarrow 2\gamma$ from Eq. 6.11 then gives the gamma ray emissivity as

$$q_\gamma = 4\pi\, \sigma_{pp} Z_{p\pi^0} \int_{E_\gamma}^{\infty} \frac{2}{E_\pi} N_0(E_\pi) \mathrm{d}E_\pi = 4\pi\, \sigma_{pp} \left\{ \frac{2 Z_{p\pi^0}}{\alpha} \right\} N_0(E_\gamma), \tag{11.2}$$

where the differential flux of nucleons, $N_0(E_\gamma)$, is now to be evaluated at the energy of the gamma ray and α is the differential spectral index of the spectrum of nucleons in the interstellar medium.

It is interesting to estimate from Eq. 11.2 the total γ-ray luminosity of the Milky Way galaxy in the simple picture of cosmic ray propagation discussed in Chapter 9. The luminosity (energy per unit time) is

$$\mathcal{L}_\gamma \approx n_H \, V_{MW} \int_{0.1\,\mathrm{GeV}} E_\gamma q_\gamma(E_\gamma) \mathrm{d}E_\gamma \approx 10^{39}\,\mathrm{erg/s}. \tag{11.3}$$

The numerical estimate is for $V_{MW} = 200\,\mathrm{pc} \times \pi\,(15\,\mathrm{kpc})^2$ and assuming a uniform density of gas equivalent to 1 hydrogen atom per cm^3 throughout the disk. The lower limit on the gamma ray energy allows us to make the power-law approximations to evaluate the integral and obtain the numerical estimate. A detailed accounting of the energy budget of the Milky Way using GALPROP is given in Ref. [342].

11.1.1 Kinematics of $p \rightarrow \pi^0 \rightarrow \gamma\gamma$

It is only at high energy ($E_\gamma > m_\pi$) that kinematic limits on the energies of the secondary photons from π^0 decay can be neglected as we have done in Eq. 11.3. At lower energy, the spectrum of photons from decay of neutral pions has a structure sometimes called the π^0 peak. Whenever the production of a secondary particle is characterized by a mass scale (in this case the mass of the $\pi^0 \approx 140$ MeV) the production spectrum has a characteristic peak that reflects the mass scale. We have already seen a more complicated example of this phenomenon, which is the peak in the spectrum of secondary antiprotons described in Section 9.3.3 and in Figure 9.4. In that case, the mass scale of ~ 2 GeV reflects the threshold for production of a nucleon–anti-nucleon pair as required by conservation of baryon number. We discuss the simpler case of $\pi^0 \rightarrow \gamma\gamma$ first, followed by the details of $\bar{p}$ production.

In the rest frame of the π^0, the two photons are produced back to back with energy $E^\star_\gamma = m_\pi/2 \approx 70$ MeV. For decay in flight the laboratory energy of the each photon is boosted according to Eq. 6.7. Because the decay is isotropic in the pion rest frame, the distribution of lab energies $\mathrm{d}n_\gamma/\mathrm{d}E_\gamma$ is flat (see discussion of Eq. 6.8). The limits are determined by $\cos\theta^\star = \pm 1$, where $\theta^\star$ is the decay angle in the pion rest frame. They are

$$\frac{m_\pi}{2}\sqrt{\frac{1-\beta}{1+\beta}} \leqslant E_\gamma \leqslant \frac{m_\pi}{2}\sqrt{\frac{1+\beta}{1-\beta}}, \tag{11.4}$$

where β is the velocity of the parent pion. The geometric mean energy of photons from decay in flight of neutral pions is $m_\pi/2 \approx 70$ MeV independent of the energy of the parent pion. Thus the composite distribution of photons from decay of an arbitrary distribution of parent pions is symmetric about 70 MeV when plotted *vs* $\ln(E_\gamma)$. It consists of a weighted sum of boxes $\mathrm{d}n_\gamma/\mathrm{d}E_\gamma$, as illustrated in Figure 11.1 and originally pointed out by Stecker [343]. A photon with energy less than $m_\pi/2$ must be a backward decay product of a moving parent pion. For $E_\gamma < m_\pi/2$, the lower the energy of the photon, the higher the energy of the parent pion must be. In fact, as derived in [343], the minimum total pion energy (rest mass plus kinetic) needed to produce a photon of energy E_γ is

$$E_\pi(\mathrm{min}) = E_\gamma + \frac{m_\pi^2}{4\,E_\gamma} \tag{11.5}$$

for any value of E_γ (either greater than or less than 70 MeV).

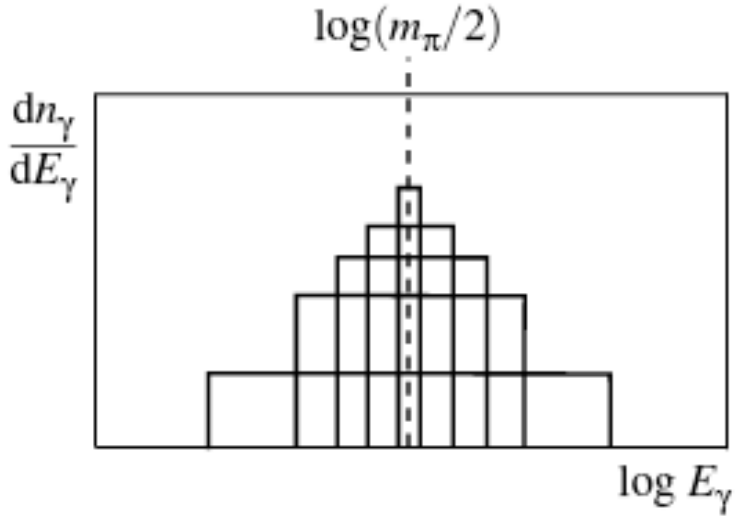

Figure 11.1 Schematic construction of the photon spectrum produced by decay of a spectrum of neutral pions.

Interactions of protons of a certain energy will produce a symmetric distribution of photons that reflects the shape of the spectrum of π^0's from nucleon interactions of that energy. A weighted sum of these distributions in turn gives the distribution of photons from a spectrum of nucleons, and the result is again symmetric in logarithmic variables. This is illustrated in Figure 11.2(b). Because each component of the distribution is symmetric about $m_\pi/2$, the distribution of photons from any composite distribution of parent π^0's peaks at $\ln(m_\pi/2)$.

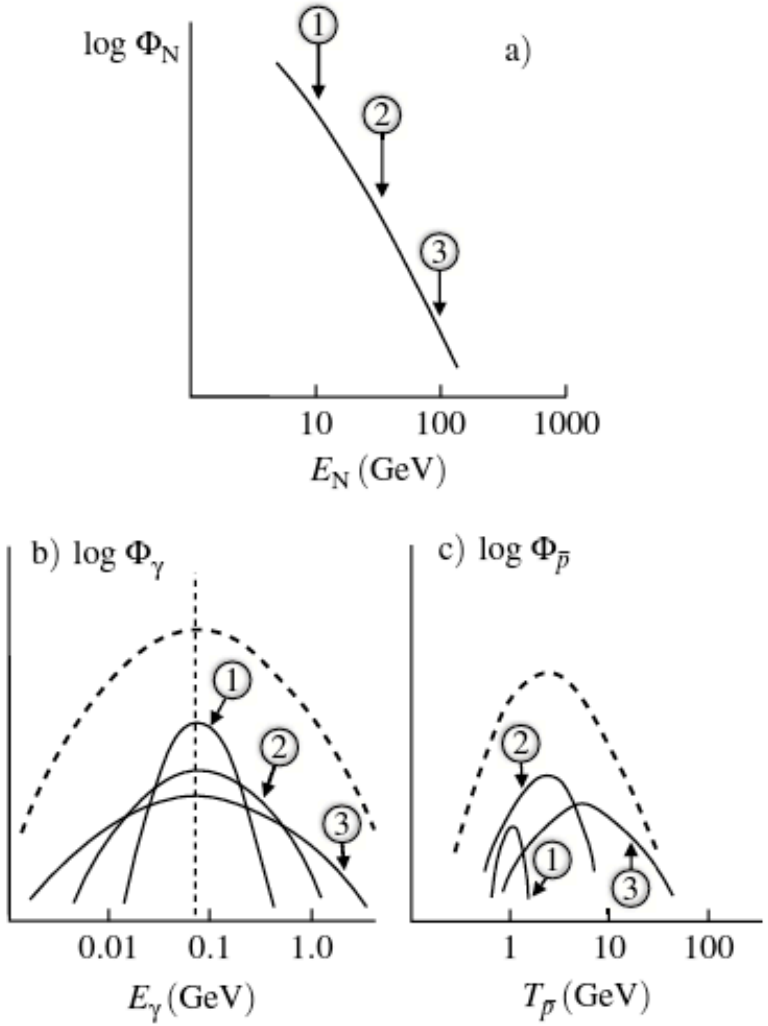

Figure 11.2 Schematic construction of spectra of secondary particles due to a spectrum of primary nucleons. For each point labelled on the primary spectrum (a), one obtains the distributions of secondaries shown in (b) for photons from π^0-decay. Part (c) of the figure shows the construction of a spectrum of antiprotons.

11.1.2 Kinematics of $p\,p \to p\,p\,p\,\bar{p}$

To treat antiprotons (or other massive secondaries) we need to consider a Lorentz transformation from a system in which particle production is symmetric back to the lab frame. The lab energy of the particle of interest is given by Eq. 6.7, here written as

$$E = \gamma\,(E^* + \beta\sqrt{(E^*)^2 - m_p^2}\,\cos\theta^*), \tag{11.6}$$

where E^* is the total energy of the secondary particle in the symmetry system. The lab energy of the secondary is bounded by Eq. 11.6 with $\cos\theta^* = \pm 1$:

$$\gamma\,E^* - \sqrt{\gamma^2-1}\sqrt{(E^*)^2 - m_p^2} \leqslant E \leqslant \gamma\,E^* + \sqrt{\gamma^2-1}\sqrt{(E^*)^2 - m_p^2}. \tag{11.7}$$

For antiprotons the symmetry system is the center of mass system of the parent nucleon-nucleon collision. Thus the Lorentz factor in Eqs. 11.6 and 11.7 is

$$\gamma = \sqrt{s}\,/\,2m_p. \tag{11.8}$$

Because of conservation of baryon number in hadronic interactions, the minimum process for production of an antiproton is

$$p\,p \to p\,p\,p\,\bar{p}. \tag{11.9}$$

The center of mass threshold for $\bar{p}$ production is therefore

$$\sqrt{s_{\text{th}}} = \sqrt{2\,m_p\,E_{\text{th}} + 2m_p^2} = 4\,m_p. \tag{11.10}$$

Thus $E_{\text{th}} = 7\,m_p$ is the threshold (total) energy that an incident proton must have in the lab system to produce an antiproton. From Eqs. 11.8 and 11.10, the Lorentz factor at threshold is $\gamma_{\text{th}} = 2$.

At threshold, the antiproton is produced at rest in the c.m., and $E^* = m_p$. Then from Eq. 11.6 the antiproton has a unique energy in the lab frame, $E_{\bar{p}} = 2m_p$, or a kinetic energy of one proton mass. To get an antiproton with kinetic energy less than 938 MeV requires that it be produced in the backward c.m. hemisphere of a higher-energy collision. Taking into account the kinematic limit for antiproton production in a nucleon–nucleon collision, a good approximation for the minimum kinetic energy of a $\bar{p}$ that can be produced by the interaction of a proton with total lab energy E_p is [344]

$$T_{\bar{p}} \approx \frac{m_p^2}{E_p - 6\,m_p}. \tag{11.11}$$

Since the cosmic ray flux decreases with increasing energy, and since the production spectrum of $\bar{p}$'s is strongly peaked around $E^* \approx m_p$, the spectrum of antiprotons produced by cosmic ray collisions in the interstellar medium will decrease for kinetic energies less than 938 MeV. The analysis that leads to this result is actually a more complicated version of that for $\pi^0 \rightarrow 2\,\gamma$, as illustrated in Figure 11.2(c). An antiproton produced near rest in the center of mass (i.e. in the peak of the distribution) will have a lab energy

$$E_{\bar{p}} \sim \gamma\, m_p = \frac{1}{2}\sqrt{2m_p E_p + 2m_p^2}, \tag{11.12}$$

Unlike the case for $\pi^0 \rightarrow 2\gamma$, the peak of the secondary distribution moves with energy.

To summarize this digression on kinematics, both photons and antiprotons produced in inelastic collisions of cosmic ray nucleons with the interstellar gas have a distinctive kinematic feature in their energy spectra. It is a peak in the spectrum related to the mass scale associated with the production. For photons the peak is at 70 MeV, and for antiprotons it is around 2 GeV kinetic energy.

11.2 Production of gamma rays by electron bremsstrahlung

For bremsstrahlung by electrons, the source function for secondary photons is written as

$$q_k(E_\gamma, \vec{r}) = \int \frac{\mathrm{d}\sigma_{e\to\gamma}(E_\gamma, E_e)}{\mathrm{d}E_\gamma} n_H(\vec{r}) \times 4\pi\phi_e(E_e)\mathrm{d}E_e, \tag{11.13}$$

where ϕ_e is the differential spectrum of electrons, n_H is the density of hydrogen in the interstellar medium and the factor of 4π accounts for the assumed isotropy of the electron spectrum. The cross section for bremsstrahlung is

$$\frac{\mathrm{d}\sigma_{e\to\gamma}(E_\gamma, E_e)}{\mathrm{d}E_\gamma} = \frac{1}{E_e} \frac{\phi(v)}{N_A X_0}, \tag{11.14}$$

where X_0 is the radiation length and $v \equiv E_\gamma/E_e$. The bremsstrahlung function, $\phi(v)$, is defined in Eq. 5.13. For a power law differential energy spectrum with index α for electrons, it is possible to show that

$$q_{e\to\gamma} \approx \frac{4\pi\rho}{X_0} \phi_e(E_\gamma) \left(\frac{1}{\alpha+1} + \frac{1.35}{\alpha-1} - \frac{1.35}{\alpha} \right). \tag{11.15}$$

The bremsstrahlung spectrum is proportional to the parent electron spectrum down to energies much less than the energy of 70 MeV at which the photon spectrum from π^0 decay peaks. This is because the only scale in the problem is the electron mass. Therefore, unless the source function for photons from electrons is very much less than that from π^0's, bremsstrahlung will dominate on the low-energy side of the peak.

We can use Eqs. 11.2 and 11.15 to express the ratio of bremsstrahlung photons to π^0 photons for power law spectra at high energy ($E_\gamma \gg 70$ MeV). It is

$$\frac{e \to \gamma}{\pi^0 \to \gamma} = \left[\frac{1}{N_A X_0 \sigma_{pp}^{\text{inel}}}\right] \left[\frac{\alpha}{2Z_{N\to\pi^0}} \left(\frac{1}{\alpha+1} + \frac{1.35}{\alpha-1} - \frac{1.35}{\alpha}\right)\right] \left[\frac{\phi_e}{\phi_N}\right]$$
$$\approx [0.85]\,[27 \times (0.6)] \left[\frac{\phi_e}{\phi_N}\right]. \qquad (11.16)$$

The square brackets group the expression into three distinct factors. The first is the ratio of interaction lengths for the two processes, which is about one. The second factor is the ratio of the spectrum weighted moments of the inclusive cross sections. Bremsstrahlung is more than an order of magnitude more efficient for the spectral index chosen in this example, $\alpha = 2.6$. The ratio of the electron spectrum to the nucleon spectrum in the few GeV energy range is somewhat less than 1%. Thus for $E_\gamma > 1$ GeV, photons from nuclear interactions (*via* π^0 decay) dominate by an order of magnitude. At lower energy, however, we expect the bremstrahlung to dominate. This is a plausible interpretation of the data, as shown in Figure 11.3.

gamma-ray flux

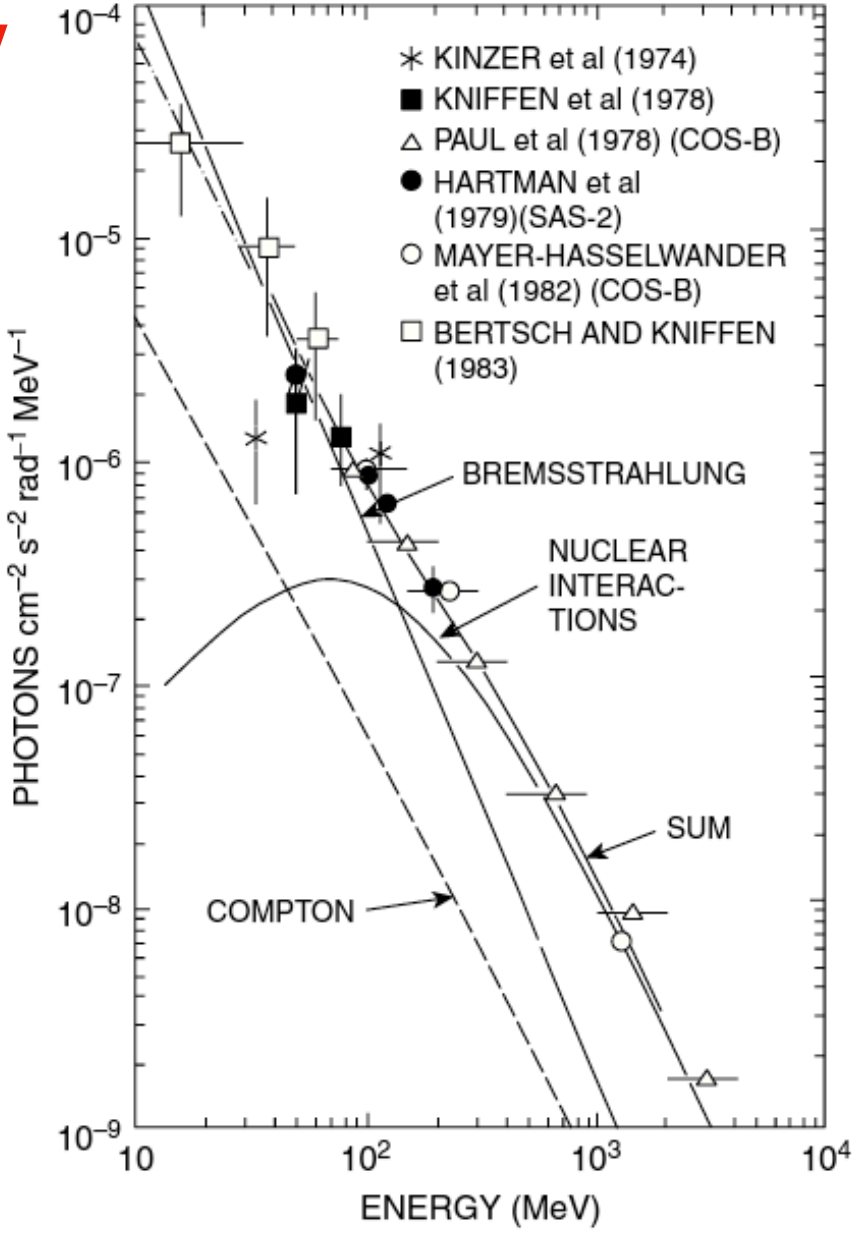

Figure 11.3 Compilation of data and comparison with calculation of gamma rays from the direction near the galactic center. (From Ref. [345].)

11.3 Diffuse γ-rays from the Galactic plane

The most extensive and sensitive studies of gamma rays in the Galaxy come from the Fermi Satellite. For example, a systematic analysis of the diffuse measurements after subtracting point sources is given in the context of GALPROP models in

Ref. [346]. Here we consider only the largest contribution, which is from $p+\text{gas} \rightarrow \pi^0 \rightarrow \gamma\gamma$. The emissivity $q_\gamma(E_\gamma)$ from Eq. 11.2 gives the total rate of gamma ray production per hydrogen atom. The emissivity in Ref. [346] is given per steradian, which differs by a factor of 4π from Eq. 11.2. If we assume the nucleon spectrum in the ISM is the same as that measured on Earth (Eq. 5.8) and take $\sigma_{pp} = 30$ mb, then we estimate the emissivity per hydrogen atom as

$$\frac{E_\gamma q_\gamma(E_\gamma)}{4\pi} = \mathcal{E}_\gamma(E_\gamma) \approx 1.4 \times 10^{-27} \left(E_{\text{GeV}}\right)^{-1.7} \text{s}^{-1}\text{sr}^{-1}. \qquad (11.17)$$

This is somewhat lower than the total emissivity (including radiation from electrons) given in Figure 34 of the Fermi paper [346].

The Astrophysical Journal, 750:3 (35pp), 2012 May 1 doi:10.1088/0004-637X/750/1/3

FERMI-LAT OBSERVATIONS OF THE DIFFUSE γ-RAY EMISSION: IMPLICATIONS FOR COSMIC RAYS AND THE INTERSTELLAR MEDIUM

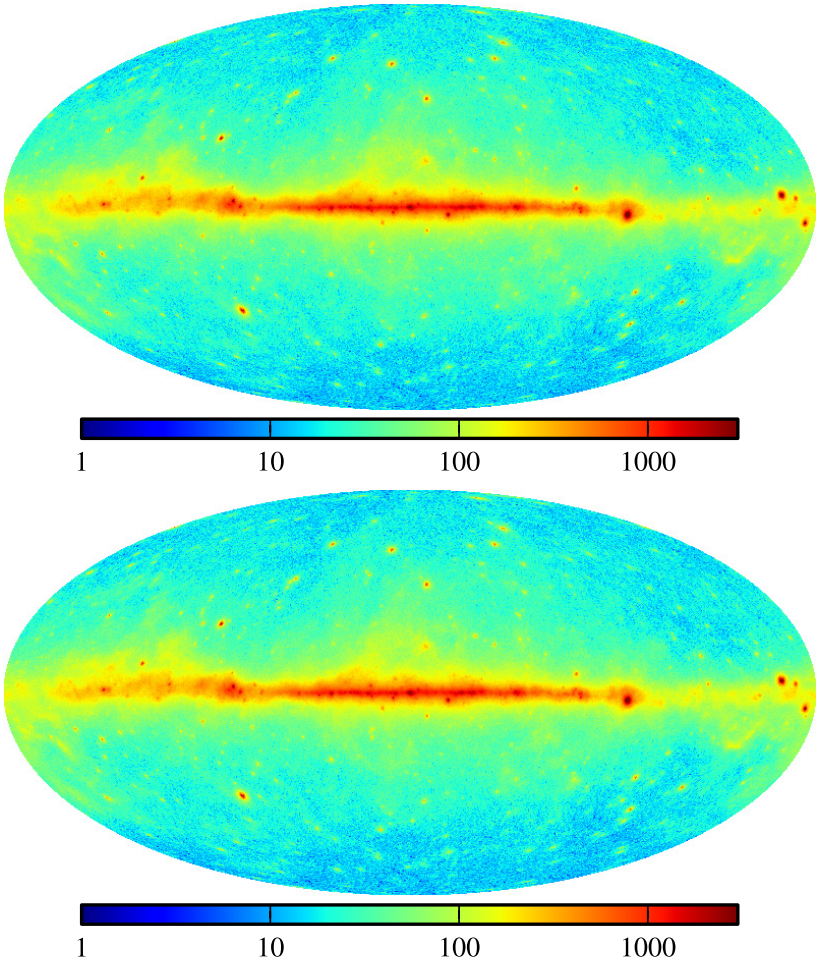

Figure 5. Upper panel: observed *Fermi*-LAT counts in the energy range 200 MeV–100 GeV used in this paper. Lower panel: predicted counts for model ${}^{S}S^{Z}4^{R}20^{T}150^{C}5$ in the same energy range. To improve contrast we have used a logarithmic scale and clipped the counts/pixel scale at 3000. The maps are in Galactic coordinates in Mollweide projection with longitudes increasing to the left and the Galactic center in the middle.

THE ASTROPHYSICAL JOURNAL, 750:3 (35pp), 2012 May 1 doi:10.1088/0004-637X/750/1/3

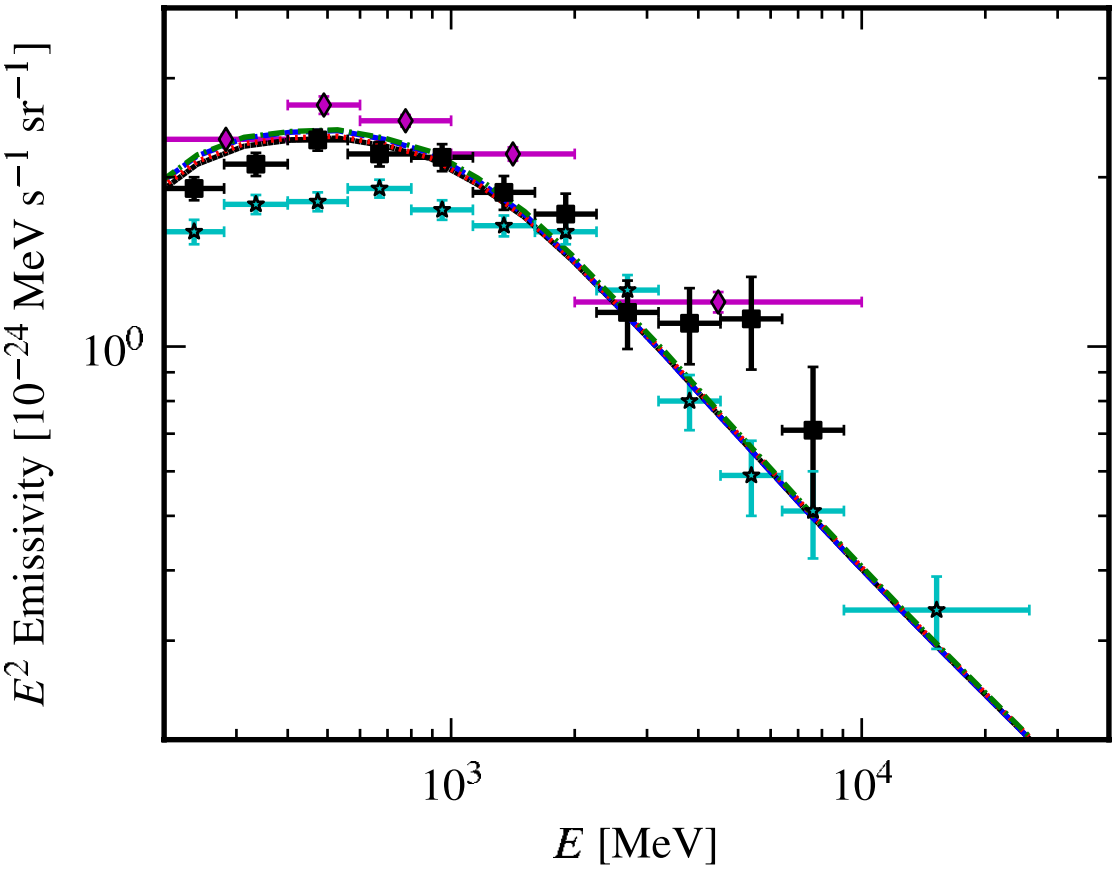

Figure 34. Average emissivity of the local annulus for model ${}^{S}S^{Z}4^{R}20^{T}150^{C}5$ (solid black), ${}^{S}L^{Z}6^{R}20^{T}\infty^{C}5$ (blue dashed), ${}^{S}Y^{Z}10^{R}30^{T}150^{C}2$ (red dotted), and ${}^{S}O^{Z}8^{R}30^{T}\infty^{C}2$ (green dash-dotted). Shown for comparison are emissivities derived from *Fermi*-LAT data using a template fitting approach. Cyan stars are from Ackermann et al. (2011b), magenta diamonds are from Abdo et al. (2010d), and black squares are from Abdo et al. (2009b).

It is also important to evaluate the π^0 contribution to the diffuse γ-ray flux produced by cosmic rays interacting with gas in the disk of the Galaxy. The rate of γ-rays per unit detector area from a small volume of space $\mathrm{d}^3\vec{r}$ is

$$\frac{\mathrm{d}\phi_\gamma}{\mathrm{d}E_\gamma \mathrm{d}A\mathrm{d}t\mathrm{d}^3\vec{r}} = \frac{q_\gamma n_H(\vec{r})}{4\pi r^2}, \tag{11.18}$$

where $n_H(\vec{r})$ is the gas density expressed as equivalent hydrogen atoms per cm^3. The observed differential flux will be an integral of contributions from all distances. Replacing $\mathrm{d}^3\vec{r}$ by $\mathrm{d}\Omega r^2\mathrm{d}r$, we can write

$$\frac{\mathrm{d}\phi_\gamma}{\mathrm{d}E_\gamma \mathrm{d}A\mathrm{d}t\mathrm{d}\Omega} = \int_0^\infty \frac{q_\gamma(r) n_H(r)}{4\pi r^2} r^2 \mathrm{d}r. \tag{11.19}$$

The spatial dependence of the integrand has two sources: one is the distribution of cosmic rays in the Galaxy $(q(r) \propto \phi_N(E, r))$ and the other is the distribution of gas, $n_H(r)$. The observed flux is a convolution of the two. If we assume the distribution of cosmic rays is the same everywhere in the gaseous disk as on Earth, then ϕ_N is a constant factor and the differential flux from a given direction is proportional to the column density of gas in that direction. Then

$$\frac{\mathrm{d}\phi_\gamma(E_\gamma, \ell, b)}{\mathrm{d}E_\gamma \mathrm{d}A\mathrm{d}t\mathrm{d}\Omega} = \frac{q_\gamma(E_\gamma)}{4\pi} \int_0^\infty n_H(r)\mathrm{d}r, \tag{11.20}$$

where the integral is the column density in a direction defined by Galactic latitude, longitude $= (b, \ell)$. For example, in a direction for which the gas density is constant at $n_H = 1\ \mathrm{cm}^{-3}$ for 1 kpc and vanishes at larger distance,

$$E_\gamma \frac{\mathrm{d}\phi_\gamma}{\mathrm{d}E_\gamma \mathrm{d}A\mathrm{d}t\mathrm{d}\Omega} \approx 4 \times 10^{-6} (E_{\mathrm{GeV}})^{-1.7} \mathrm{cm}^{-2}\mathrm{s}^{-1}\mathrm{sr}^{-1}. \tag{11.21}$$

To compare with the Fermi observations, we calculate the π^0 contribution to the diffuse flux from the inner galaxy (Figure 17 of Ref. [346]). The Fermi observation is averaged over $-8^\circ < b < 8^\circ$ in Galactic latitude and over $-80^\circ < \ell < +80^\circ$ in longitude. To compare with this measurement, we have to average Eq. 11.20 over the region shown in Figure 11.4 with a half-angle of the wedge of 8°. If we assume that there is no longitudinal dependence of the gas density in this region and we approximate n_H as a constant within a disk of thickness $2h$ and zero outside, then the fraction of the solid angle that gives a nonzero contribution is

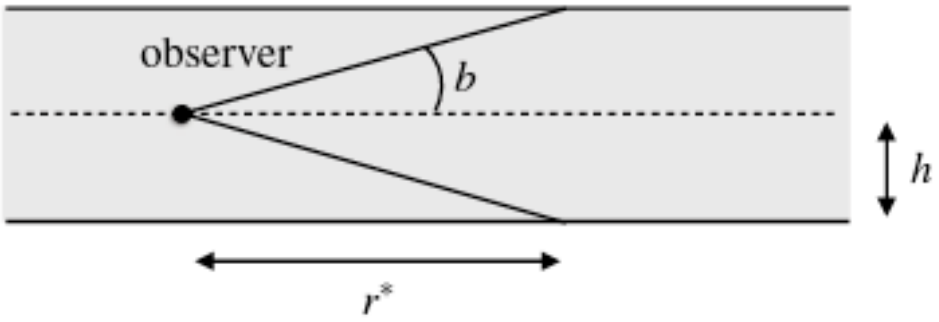

Figure 11.4 Geometry for calculating the cosmic ray-induced diffuse γ-radiation from the Galactic plane.

$$F(r) = \frac{\int_{90^\circ - b}^{90^\circ + b} \sin\theta \, H\left(\frac{h}{r} - \theta\right) \mathrm{d}\theta}{2b}, \tag{11.22}$$

where the Heaviside function $H\left(\frac{h}{r} - \theta\right)$ enforces the boundary condition of the simple model. Then

$$E_\gamma \frac{\mathrm{d}n_\gamma}{\mathrm{d}A\mathrm{d}t\mathrm{d}E_\gamma\mathrm{d}\Omega} = \mathcal{E}_\gamma(E_\gamma) \left\{ \int_0^{r^*} \mathrm{d}r + \int_{r^*}^{r_{\max}} \frac{h}{b}\frac{\mathrm{d}r}{r} \right\}, \tag{11.23}$$

where $r^* = h/\tan b \approx 7\,h$. The factor in curly brackets gives the fraction of the Galactic latitude as a function of distance from which signal is received in the simple model with constant density inside and no gas above h. Performing the integrals gives

$$\begin{aligned} \frac{E_\gamma \mathrm{d}n_\gamma}{\mathrm{d}A\mathrm{d}t\mathrm{d}E_\gamma\mathrm{d}\Omega} &= \mathcal{E}_\gamma(E_\gamma) \times 7h \left\{ 1 + \ln\left(\frac{R_{\max}}{7h}\right) \right\} \qquad (11.24) \\ &\approx 10^{-5}\,\mathrm{cm}^{-2}\mathrm{s}^{-1}\mathrm{sr}^{-1} \left(\frac{h}{100\,\mathrm{pc}}\right) \left(\frac{n_H}{\mathrm{cm}^{-3}}\right) \left(\frac{E_\gamma}{\mathrm{GeV}}\right)^{-1.7}. \end{aligned}$$

This level agrees with the Fermi result for $h = 200$ pc with $\langle n_H \rangle = 1\ \mathrm{cm}^{-3}$ or $h = 100$ pc with $\langle n_H \rangle = 2\ \mathrm{cm}^{-3}$.

The Astrophysical Journal, 750:3 (35pp), 2012 May 1 doi:10.1088/0004-637X/750/1/3

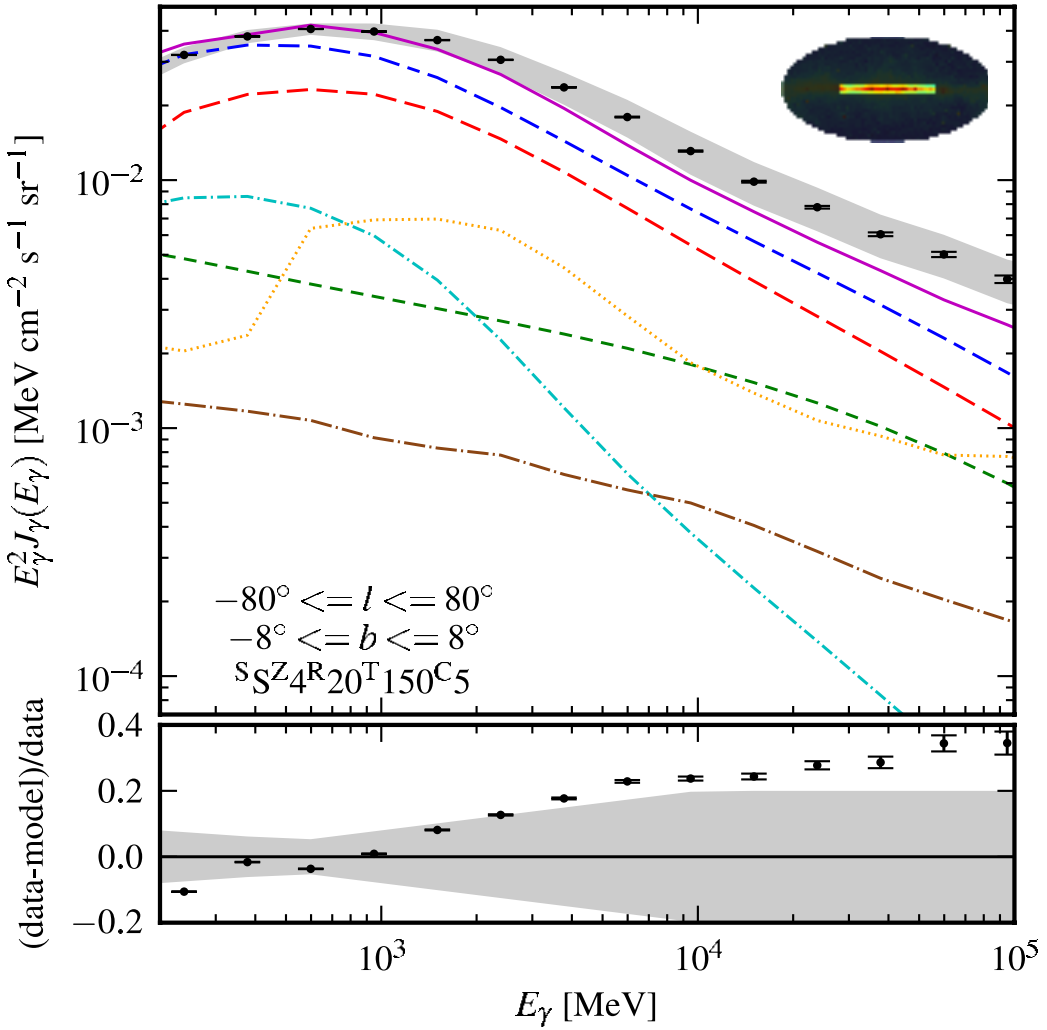

total incl. sources

total diffuse galactic emission

pion decay

detected sources

inverse Compton

isotropic background

bremsstrahlung

Figure 17. Spectra extracted from the inner Galaxy region for model $^{S}S^{Z}4^{R}20^{T}150^{C}5$ using Pass 7 clean photons. The dip between 10 and 20 GeV is greatly reduced compared to Figure 15. See Figure 12 for legend.

11.4 Neutrinos from the Galactic plane

Neutrinos are produced along with gamma rays from charged pions and kaons produced in the same cosmic ray interactions that give rise to the neutral pion contribution to the diffuse gamma radiation. Since neutrinos are produced only through hadronic processes, a measurement of secondary neutrinos from the Galactic plane would give an independent constraint on the relative contribution of neutral pions and electrons to the observed flux of gamma rays from the Galactic plane. In fact, however, the background of atmospheric neutrinos makes such a measurement very difficult.

An early calculation by Stecker [347] points out that the spectrum of the diffuse neutrinos from the Galactic plane will have the same spectrum as the cosmic ray spectrum and will therefore eventually, at sufficiently high energy, be larger than the atmospheric background. The crossover is, however, above 100 TeV where the neutrino fluxes are already exceedingly low.

The starting point for a calculation is the neutrino luminosity per hydrogen atam, analogous to Eq. 11.2, which is more complicated because of the decay chains involved. The factor $2Z_{p\pi^0}/\alpha \approx 0.031$ is the product of the spectrum weighted moment for π^0 production times the moment of the distribution for the decay $\pi^0 \to 2\gamma$. The corresponding factor for $\nu_e + \bar{\nu}_e$ is

$$(Z_{p\pi^+} + Z_{p\pi^-}) \left(\frac{1 - r_\pi^\alpha}{\alpha(1 - r_\pi)} \right) (\langle y^{\alpha-1} \rangle_0^{\nu_e} + f(r_\pi) \langle y^{\alpha-1} \rangle_1^{\nu_e}) \approx 0.0102, \quad (11.25)$$

where the $\langle y \rangle$ moments are defined in the second row of Table 6.3, and $f(r_\pi)$ is the coefficient of $\langle y^{\alpha-1} \rangle_1$ in Eq. 6.65. The factors correspond respectively to $p \to \pi^\pm$, $\pi^\pm \to \mu^\pm$ and $\mu^+ \to e^+ \bar{\nu}_\mu \nu_e$ (and the corresponding μ^- decay contribution).

The expression for $\nu_\mu + \bar{\nu}_\mu$ is still more complicated because the two-body decays of charged pions and kaons have to be accounted for in addition to the muon contribution. The full expression is

$$\begin{aligned} & (Z_{p\pi^+} + Z_{p\pi^-}) \frac{(1 - r_\pi)^\alpha}{\alpha(1 - r_\pi)} \approx 0.0069 \quad (11.26) \\ & + \left(\frac{1 + \delta_0}{2} Z_{pK^+} + \frac{1 - \delta_0}{2} Z_{nK^+} + Z_{pK^-}\right) \frac{(1 - r_K)^\alpha}{\alpha(1 - r_K)} \approx 0.0039 \\ & + (Z_{p\pi^+} + Z_{p\pi^-}) \frac{1 - r_\pi^\alpha}{\alpha(1 - r_\pi)} (\langle y^{\alpha-1} \rangle_0^{\nu_\mu} + f(r_\pi) \langle y^{\alpha-1} \rangle_1^{\nu_\mu}) \approx 0.0105 \\ & \approx 0.0213. \end{aligned}$$

The small contribution of kaons to production of muons has been neglected here. Because of the low density of the ISM, the kaon contribution to muons is at the low energy value of $\approx 5\%$ (Figure 6.5). In round numbers, we have $(\nu_\mu + \bar{\nu}_\mu) / \gamma \approx 2/3$ and $(\nu_e + \bar{\nu}_e) / \gamma \approx 1/3$ at production.

As an example, we calculate the flux of $\nu_\mu + \bar{\nu}_\mu$ from the inner galaxy defined in the same way as for the Fermi diffuse gamma rays discussed in the previous section. The angular range is Galactic coordinates of $-8^\circ < b < +8^\circ$ and $-80^\circ < \ell < +80^\circ$ corresponds to a total solid angle of 0.78 sr. The Fermi result for π^0-produced photons in this region corresponds to a normalization at 1 GeV of $2 \times 10^{-5}\text{cm}^{-2}\text{sr}^{-1}\text{s}^{-1}$. If we extrapolate with an integral spectral index of -1.7 and use the ν/γ production ratio from Eq. 11.26, the expected neutrino flux from the Galactic center region is

$$\phi_\nu = \frac{\mathrm{d}N_\nu}{\mathrm{d}E_\nu} \approx \frac{1}{2} \times 1.3 \times 10^{-5} E_\nu^{-1.7}\,\mathrm{cm}^{-2}\mathrm{sr}^{-1}\mathrm{s}^{-1}. \tag{11.27}$$

The factor $1/2$ estimates the survival probability of ν_μ due to neutrino oscillations. The corresponding rate of ν_μ-induced muons is

$$R_{GP} \sim 0.78\,\mathrm{sr} \times 10^{10}\mathrm{cm}^2 \int \phi_\nu\, P(E_\nu, E_\mu > E_{\mathrm{th}})\mathrm{d}E_\nu\,\mathrm{s}^{-1} \tag{11.28}$$

for a kilometer-scale detector. Evaluating the integral gives 28, 10 and 7 events per year respectively for muon energy thresholds of 0.1, 1 and 10 TeV. The background from atmospheric neutrino-induced muons from the same region of the sky can be estimated by scaling from Figure 8.7. The corresponding numbers are 14, 000, 1, 900 and 500. Although the signal/background ratio is increasing with energy because of the steeper atmospheric spectrum, the signal in one year is significantly less than one sigma.

11.5 Spectrum of electrons

The electron spectrum is needed to calculate its contribution to production of gamma rays, but it is also of intrinsic interest as a probe of cosmic ray sources. Synchrotron radiation of electrons in supernova remnants is a widely used indicator of cosmic ray acceleration, and is an important probe of external galaxies as well. Propagation of electrons differs from that of protons because of the importance of radiative energy losses in galactic magnetic fields. Figure 11.5 shows the spectrum of electrons measured by AMS. At high energy it can be described by a power law with a differential spectral index of -3.2. If the electrons are produced in the same sources as protons and other nuclei and accelerated with the same spectral index, we might at first guess that the observed spectral index should also be the same. That is not the case because the electrons lose energy, primarily by inverse-Compton (IC) scattering and synchrotron radiation.

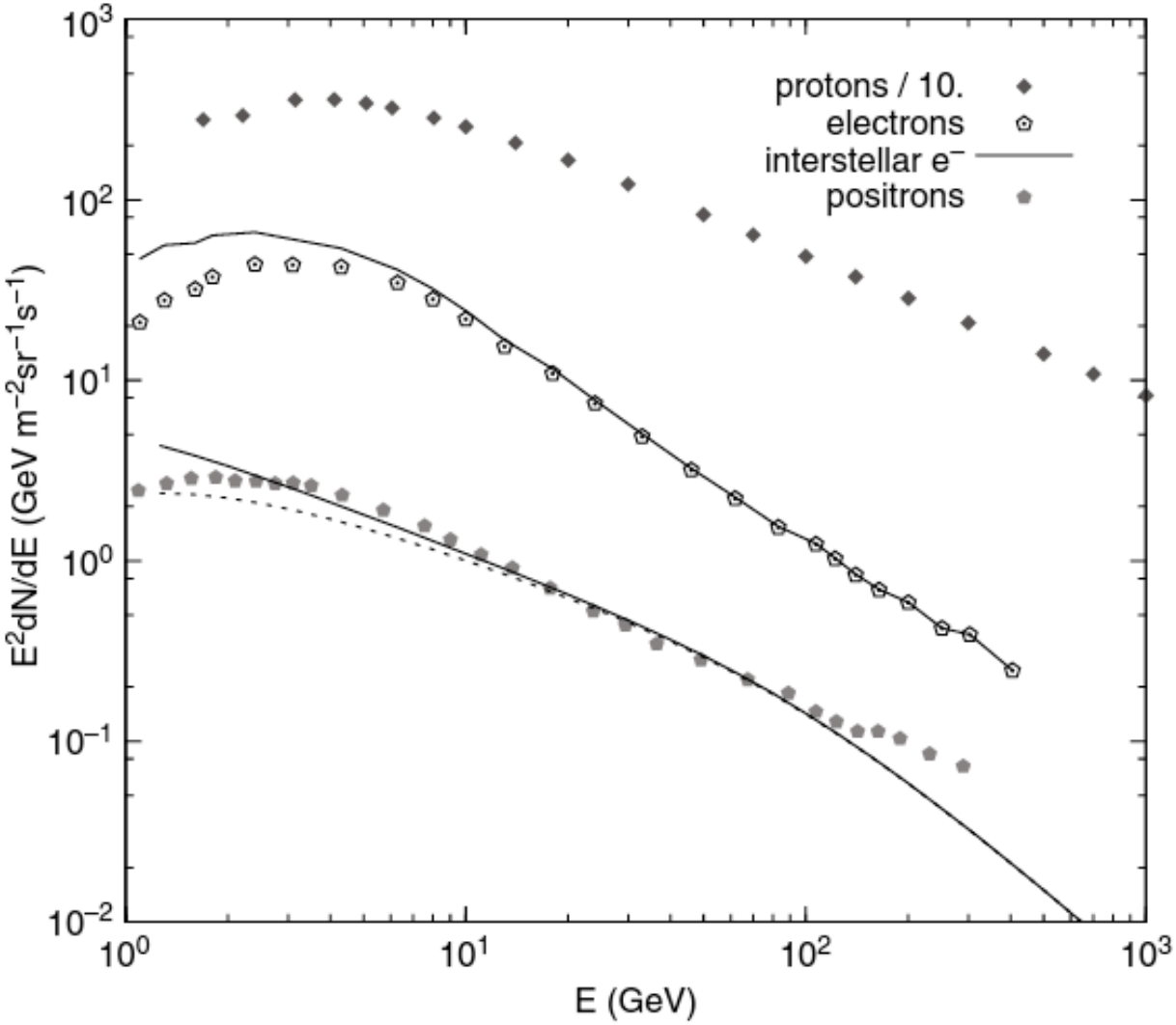

Figure 11.5 Measurements of the spectrum of electrons from AMS-02 [350]. The line shows the spectrum demodulated with a potential $\phi = 550$ MeV. Also shown are the scaled proton spectrum and the positron spectrum. The prediction of the nested leaky box model for positrons is shown by a full line. The dotted line is an estimate of the modulated prediction using $\phi = 450$ MeV.

The electron loses energy at a rate

$$\frac{\mathrm{d}E}{\mathrm{d}t} = -\beta E^2 \tag{11.29}$$

which has the solution $E(t) = E_0/(1 + \beta E_0 t)$ corresponding to an energy-dependent loss time

$$\tau_e(E) = \frac{1}{\beta E}. \tag{11.30}$$

Both IC and synchrotron losses are proportional to E^2. The IC coefficient is proportional to the energy density in target photons, which is ~ 1 eV/cm^3, comparable to the energy density in cosmic rays of 0.5 eV/cm^3. The synchrotron coefficient is proportional to the energy density of the magnetic field, $B^2/8\pi \approx 0.25$ eV/cm^3, which is also comparable to the energy density in cosmic rays. With the energy densities in eV/cm^3, the numerical coefficient β is 8×10^{-17} (GeV s)$^{-1}$ [293]. This corresponds to a characteristic time $\tau_e(E) \approx 10^{16}\,\mathrm{s}/E(\mathrm{GeV})$ during which the electron would diffuse a distance $\ell_e \approx \sqrt{D\tau_e(E)}$. For electrons of 1 GeV, this distance is ≈ 5 kpc, approximately the height of the galactic halo in the cylindrical model discussed in Chapter 9. Thus, electrons with lower energy can reach the edge of the halo without significant energy loss, but electrons of higher energy lose significant amounts of energy before escaping from the Galaxy.

Discussion: It is interesting that about 15% of the energy loss of electrons is a consequence of inverse-Compton scattering in the cosmic background radiation (CMB), which has an energy density of 0.26 eV/cm^3. This contribution to the steepening of the electron spectrum is in some sense analogous to the anticipated steepening of the cosmic ray spectrum due to photo-pion production in the CMB. An interesting early discussion of this effect is given in [348].

To see qualitatively how energy loss affects the energy spectrum, we can write the equilibrium density of electrons as a production rate per unit volume multiplied by the relevant lifetime in the containment region. Since the containment volume is larger than the source region, the emissivity in the source region, $Q(E)$, must be multiplied by the ratio of the source volume to the containment volume to get the production rate averaged over the containment volume. With a cylindrical approximation to the disk and halo this ratio is the height of the source region divided by the distance the electrons diffuse above the plane. The estimate then is

$$N_e(E) \sim Q(E) \frac{h_{\rm source}}{\ell_e(E)} \tau(E) \qquad (11.31)$$

as in [293]. In this equation, $h_{\rm source} \approx 100$ pc and $\tau(E)$ is the lifetime of electrons with energy E in the Galaxy. When $\ell_e > H$, the lifetime of electrons in the Galaxy is the same as for protons, $\sim H^2/D$ (Eq. 9.28) and $N_e(E) \propto Q(E) \times E^{-\delta}$, as for protons. (Recall that the diffusion is proportional to E^{δ}.)

When $\ell_e > H$, the lifetime of electrons in the Galaxy is the same as for protons, $\sim H^2/D$ (Eq. 9.28) and $N_e(E) \propto Q(E) \times E^{-\delta}$, as for protons. (Recall that the diffusion is proportional to E^{δ}.) For energies higher than a GeV, however, the lifetime of electrons in the Galaxy is the energy loss time from Eq. 11.30, which decreases as $1/E$. Since $\ell_e \propto \sqrt{\tau_e D}$ the net effect of the energy loss dependence of the electrons is to make the spectrum steeper by $\frac{1}{2} + \delta/2$ compared to the source spectrum. In fact, the observed electron spectrum is steeper by approximately $\frac{1}{2}$ than the *observed* spectrum of protons. The observed electron spectrum shown in Figure 11.5 can be approximated by a differential index of -3.2 from 10 to 200 GeV. We can get this slope by assuming that the source spectrum for electrons is $Q(E) \propto E^{-2.4}$, as is assumed by [349] above 10 GeV. If $\delta = 0.6$, however, then the source spectral index of protons would be 2.1, substantially different from electrons. If $\delta = 0.3$ at high energy, as in the diffusion model with reacceleration, then the difference between the injection spectra of protons and of electrons would be smaller. The full treatment of diffusive propagation of electrons requires accounting for the variation of the diffusion and energy loss processes as a function of height above the source region, as in Chapter 5 of [293].

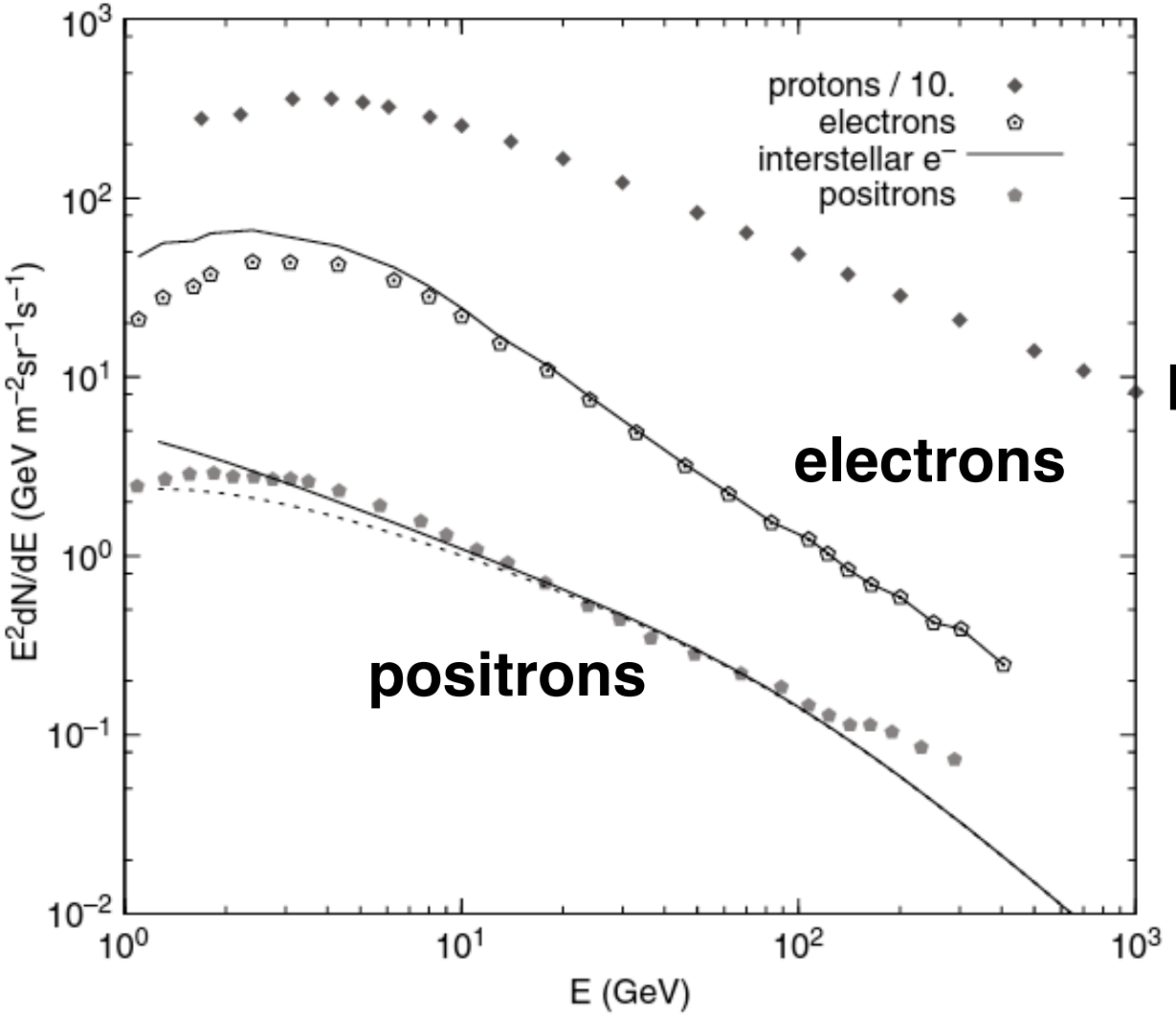

Figure 11.5 Measurements of the spectrum of electrons from AMS-02 [350]. The line shows the spectrum demodulated with a potential $\phi = 550$ MeV. Also shown are the scaled proton spectrum and the positron spectrum. The prediction of the nested leaky box model for positrons is shown by a full line. The dotted line is an estimate of the modulated prediction using $\phi = 450$ MeV.

11.6 Positrons

It is also interesting to examine the prediction of Eq. 11.31 for positrons under the assumption that there are no primary positrons from cosmic ray sources. In that case the source spectrum is known. It is generated by interactions of cosmic ray protons and nuclei producing pions which lead to positrons via the chain

$$p + H_{\mathrm{ISM}} \rightarrow \pi^+ \rightarrow \mu^+ \rightarrow e^+. \tag{11.32}$$

Since each step in the chain depends on the ratio $E_{\mathrm{in}}/E_{\mathrm{out}}$, the production spectrum of positrons has the same spectral index as the observed spectrum of protons, ≈ -2.7. Thus we get the result that the observed spectrum of secondary positrons (and secondary electrons) should be

$$N_e(E) \approx \text{const} \times E^{-(2.7+0.5+\delta/2)} \sim E^{-3.4}. \tag{11.33}$$

The normalization constant is calculated in Appendix A.9.

11.6.1 Hard spectrum of positrons

The measured spectrum of positrons is shown in Figure 11.5. Instead of the steep slope expected for secondary positrons, the observed spectrum has an index (≈ -2.7), similar to the spectrum of the protons that produce the secondary positrons. The observation by PAMELA [351] of the relatively hard spectrum of positrons and a ratio of positrons to electrons that increases at high energy was confirmed by Fermi [352] and AMS-02 [350]. This discovery has generated considerable interest because it seems to indicate that there is a primary component of positrons over and above the steep secondary spectrum.

Several sources of the hard positron spectrum have been suggested. They range from products of dark matter annihilation to creation and acceleration in pulsar wind nebulae to acceleration of secondaries produced inside the acceleration zone of supernova remnants. The review of Serpico [353] summarizes and discusses the pros and cons of various models that have been suggested. In the next subsection, we outline a model of the hard positron spectrum which, although it is a minority view, provides an instructive pedagogical exercise.

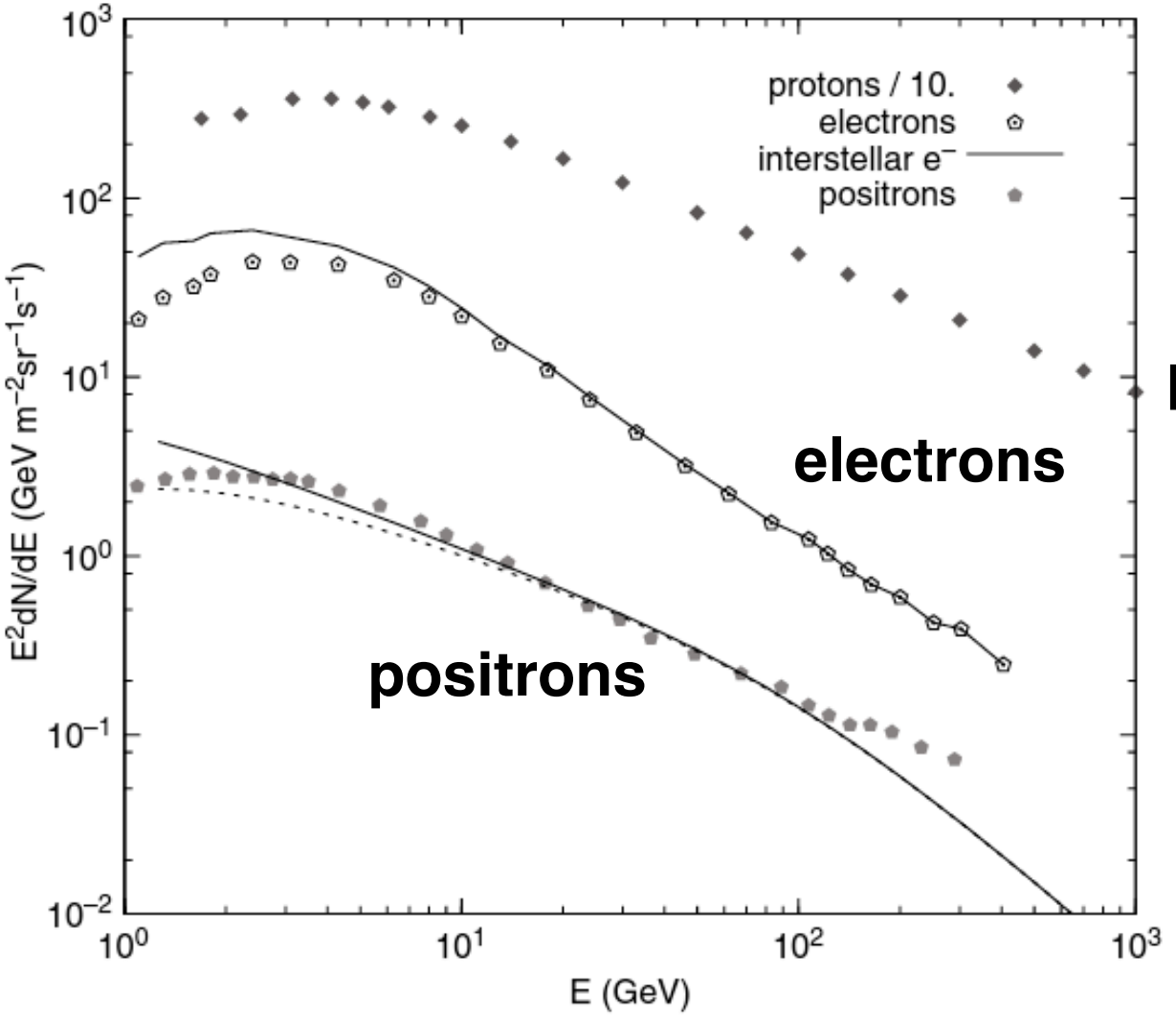

Figure 11.5 Measurements of the spectrum of electrons from AMS-02 [350]. The line shows the spectrum demodulated with a potential $\phi = 550$ MeV. Also shown are the scaled proton spectrum and the positron spectrum. The prediction of the nested leaky box model for positrons is shown by a full line. The dotted line is an estimate of the modulated prediction using $\phi = 450$ MeV.

11.7 Cosmic rays and γ-rays in external galaxies

At the beginning of this chapter we estimated the total γ-ray luminosity of the Milky Way galaxy as $\approx 10^{39}$ erg/s. The γ-ray luminosity of the Milky Way is plotted along with the luminosities of several external galaxies as a function of the rate of star formation in Figure 11.6 from the Fermi-LAT Collaboration [356]. The figure shows that γ-ray luminosities of galaxies show a good correlation with their star-forming rates, in the external galaxies and in the Milky Way.

Calculating the luminosity is not the same for all galaxies because the propagation of cosmic rays is different and is most likely correlated with the rate of star formation. The cycle of collapse of molecular gas, star formation, stellar evolution of massive stars, stellar collapse and cosmic ray acceleration is the subject of Chapter 13 for the Milky Way. The emerging evidence for a correlation between star formation rates and cosmic ray-induced γ-radiation suggests a picture in which high rates of star formation are associated with dense environments, a high rate of stellar collapse and cosmic ray acceleration (and consequently also with greater turbulence and higher magnetic fields).

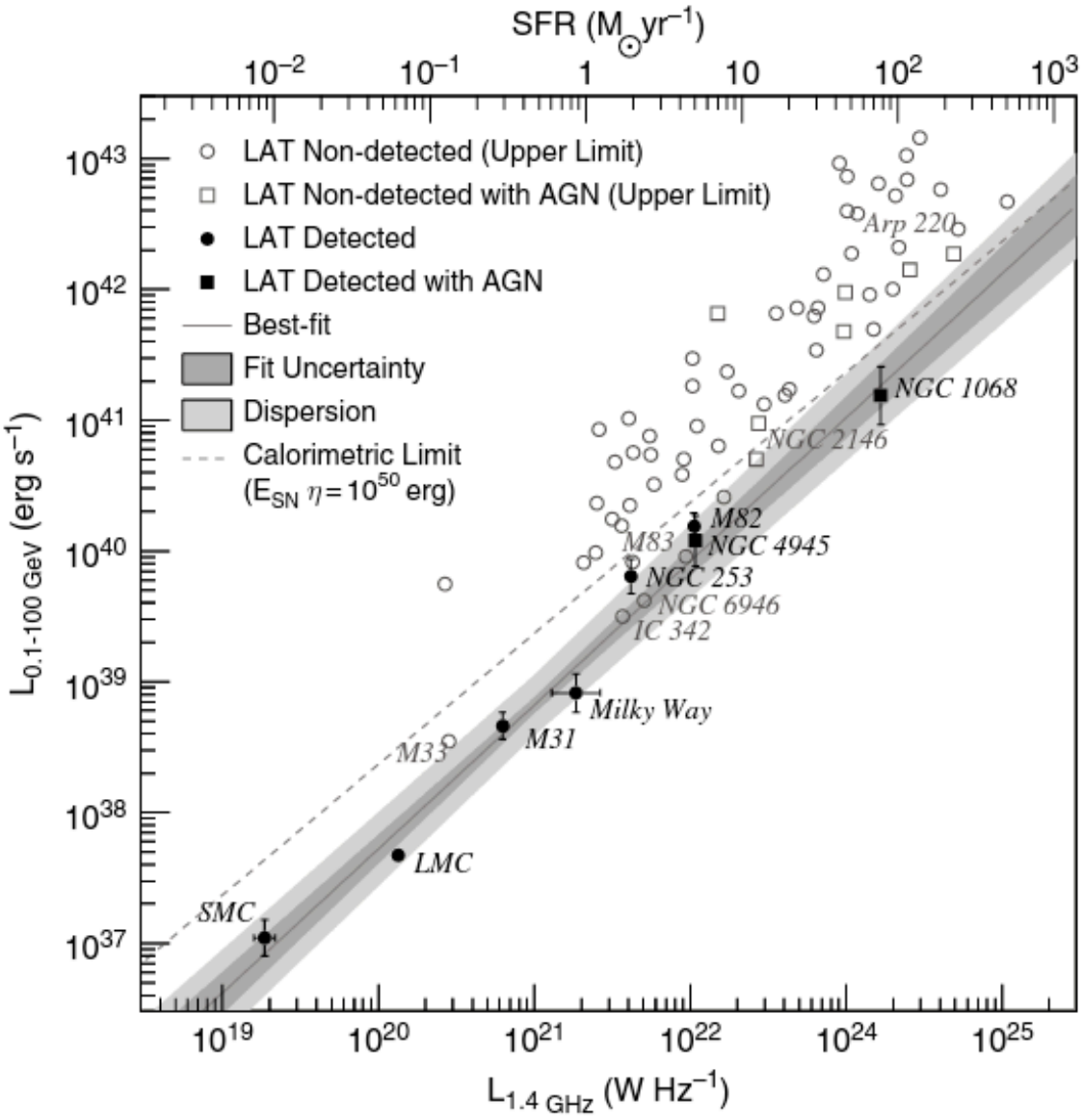

Figure 11.6 Correlation of γ-ray luminosities with rate of star formation. From [356], © 2012 by American Astronomical Society, reproduced with permission.

In galaxies with the highest rate for star formation, it is possible that the cosmic rays lose a large fraction of their energy by interactions with the dense interstellar medium before they escape. In the Milky Way only a small fraction of the cosmic rays interact to produce gamma rays. The cosmic ray spectrum in the ISM is therefore steeper than the spectrum at the accelerator. On the other hand, in the so-called "calorimetric limit" where all cosmic rays interact before diffusing out of their galaxy, the spectrum in the ISM is the same as the source spectrum. The dotted line in Figure 11.6 of the figure shows the luminosity expected in this limit. Moreover, there is a tendency for galaxies with the highest rates of star formation to have harder γ-ray spectra, as shown in Figure 11.7. Galaxies with high levels of star formation are called "starburst galaxies." We will return to a discussion of starburst galaxies in connection with neutrinos in Section 18.8.

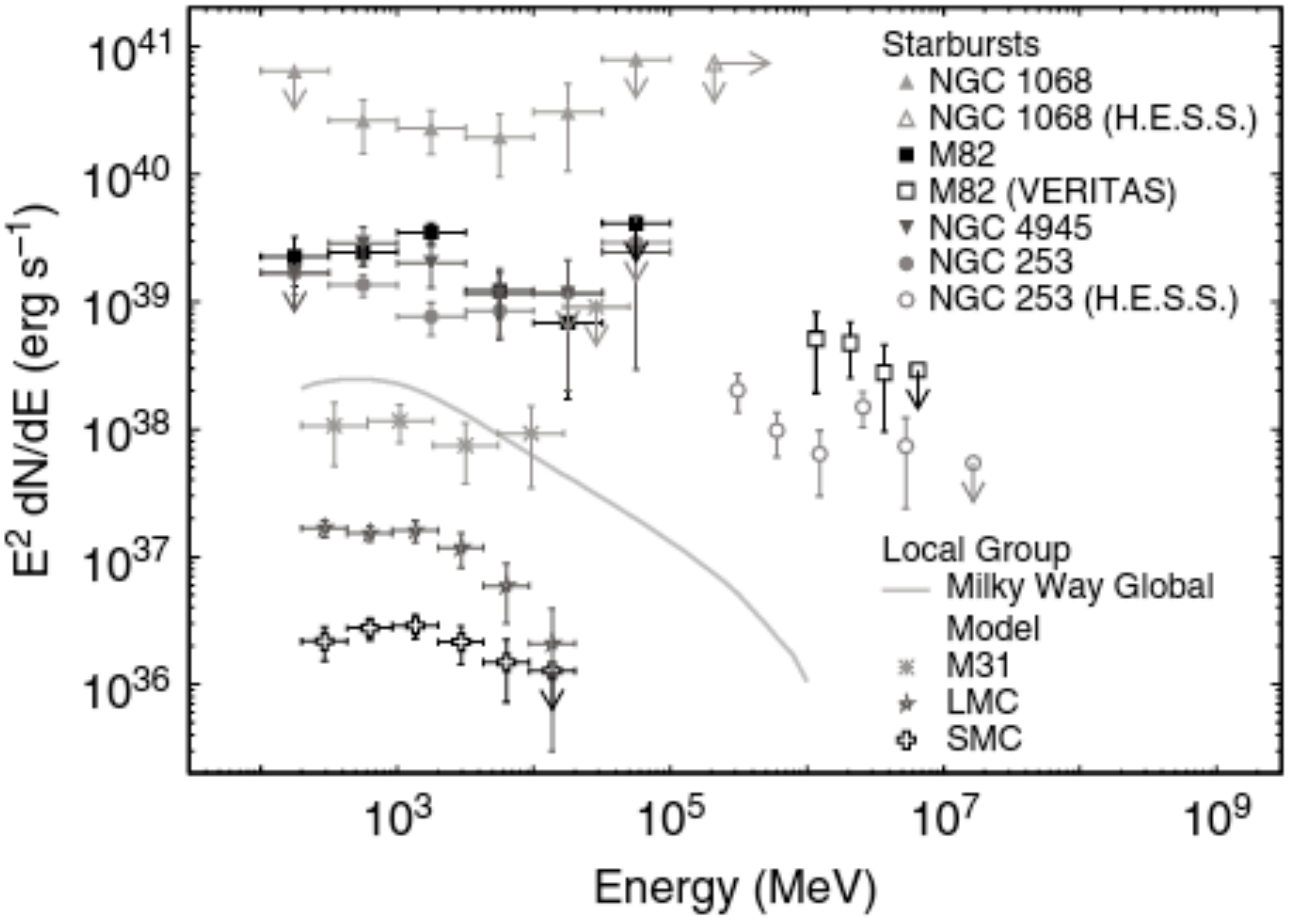

Figure 11.7 Gamma ray spectra of external galaxies inferred from measured fluxes and distances to the sources. From [356], © 2012 by American Astronomical Society, reproduced with permission.